REENTRY HEAT TRANSFER ANALYSIS OF THE SPACE SHUTTLE ORBITER

William L. Ko, Robert D. Quinn, Leslie Gong,
Lawrence S. Schuster, and David Gonzales
Dryden Flight Research Center
Edwards, California

SUMMARY

A SPAR (structural performance and resizing) finite element thermal analysis computer program was used in the reentry heat transfer analysis of the space shuttle. Two typical wing cross sections and a midfuselage cross section were selected for the analysis. The surface heat inputs to the thermal models were obtained from aerodynamic heating analyses, which assumed (1) a purely turbulent boundary layer, (2) a purely laminar boundary layer, (3) separated flow, and (4) transition from laminar to turbulent flow.

The effect of internal radiation was found to be quite significant. With the effect of the internal radiation considered, the wing lower skin temperature became about 39° C (70° F) lower.

The results were compared with flight data for STS-1 (space transportation system, trajectory 1). The calculated and measured temperatures compared well for the wing if laminar flow was assumed for the lower surface and bay 1 upper surface and if separated flow was assumed for the upper surfaces of bays other than bay 1. For the fuselage, good agreement between the calculated and measured data was obtained if laminar flow was assumed for the bottom surface. The structural temperatures were found to reach their peak values shortly before touchdown.

In addition, the finite element solutions were compared with those obtained from the conventional finite difference solutions.

INTRODUCTION

The space shuttle orbiter is designed to be used for at least 100 missions. During each flight cycle, it must withstand the vibrations of lift-off and survive severe aerodynamic heating as it reenters the atmosphere at extremely high velocity (approximately Mach 25 at the start of reentry) and high angle of attack (approximately 40° during the early phase of reentry). The space shuttle skins are constructed primarily of aluminum and/or graphite/epoxy composites, which must be protected from being heated beyond the design limit (176° C, 350° F). Overheating would result in the loss of structural integrity required for subsequent flights. Thus, a thermal protection system (TPS) is bonded to the skins. Another area of great concern is the thermal stresses. The strain isolation pad (SIP) is designed to

absorb the skin buckling effect on the TPS. If skin buckling is too severe, the TPS and the shuttle skins may debond, resulting in partial or total loss of the TPS function.

In order to gain confidence in the thermal performance of the shuttle under a prescribed reentry flight profile (time histories of velocity, altitude, and angle of attack), a preflight reentry heating thermal analysis of the space shuttle was conducted. The structural temperature distribution obtained from the thermal analysis can then be used to calculate thermal stresses for studying structural performance. The present paper is limited to the prediction of structural temperature distribution. The results are compared with flight measured data from the first flight.

ANALYSIS

For the analysis, it was assumed that the space shuttle enters the atmosphere under the nominal (or design) STS-1 (space transportation system, trajectory 1) trajectory (shown in fig. 1 (solid lines)). The flight data shown in the figure closely follow the nominal trajectory. Time zero in the analysis corresponds to the start of reentry, which is defined to occur at an altitude of 121,920 meters (400,000 feet). Based on the nominal STS-1 trajectory, the preflight aerodynamic heating was calculated using the classical aerodynamic theories and assuming several types of flow conditions (turbulent, laminar, and separated). Two typical wing cross sections, wing stations (WS's) 240 and 328, and a midfuselage cross section, fuselage station (FS) 877, were selected for the thermal analysis. The locations of WS 240, WS 328, and FS 877 are shown in figure 2.

DESCRIPTION OF STRUCTURES

The geometry of the wing segment bound by WS 240 and WS 254 is shown in figure 3. Both the upper and lower skins of bay 1 are made of aluminum honeycomb core sandwich plates. The skins of bays 2, 3, and 4 are made of hat-stringer-reinforced aluminum. The spar webs are made of corrugated aluminum plates, except for the forward spar web of bay 1, which is made of aluminum honeycomb core sandwich plates. The entire lower wing skin is covered with HRSI (high temperature reusable surface insulation), with SIP lying between the wing skin and the HRSI. Most of the upper skin of bay 1 is protected by LRSI (low temperature reusable surface insulation), under which lies the SIP layer. A small portion of the upper skin of bay 1 and the upper skins of bays 2, 3, and 4 are covered only with FRSI (felt reusable surface insulation).

The wing segment bound by WS 328 and WS 342.5 (fig. 4) has only three bays. The forward spar web of bay 1 is made of honeycomb core sandwich plate, and the rest corrugated plates. All the lower and the upper skins are hat-stringer stiffened. The lower skin is covered with HRSI, and the upper skin LRSI. No FRSI appears on the upper surface of WS 328.

The geometry of the fuselage cross section FS 877 is shown in figure 5. Both the fuselage belly and the sidewall are made of T-stiffener-reinforced aluminum. The

lower and upper skins (except for the leading edge region) are made of hat-stringer-reinforced aluminum. The leading edge region of the glove skin is made of aluminum honeycomb core sandwich structure. A small portion of the bay door inner surface is covered by an RTV (room-temperature-vulcanized) layer, which serves as a heat sink. The fuselage belly and the lower glove are protected with HRSI. The upper glove is covered partly with HRSI (region of the honeycomb core sandwich structure) and partly with LRSI. The lower portion of the sidewall is covered with FRSI, and the upper portion with LRSI. The outside surface of the bay door is protected by FRSI.

THERMAL MODELING

To account for the spanwise heat flow and the effect of the rib trusses at WS 254, the wing segment shown in figure 3 was modeled in three dimensions using a SPAR (structural performance and resizing) finite element thermal analysis computer program (ref. 1) rather than the conventional finite difference method. The entire finite element thermal model for the wing segment, shown in figure 6, has 920 joint locations (JLOC's or nodes). The modeling was limited to the major load-carrying portion (bays 1 to 4) of WS 240. In modeling, all the wing skins and the spar webs were replaced by solid plates having corresponding effective thicknesses. The equivalent wing skins and spar webs, rib cap shear webs, TPS surface coatings, and RTV layers (lying on both sides of the SIP) were then modeled using SPAR K41 elements (4-node, two-dimensional heat conduction elements). The spar caps, rib caps, and rib trusses were modeled using SPAR K21 elements (2-node, one-dimensional heat conduction elements). The TPS was modeled in 10 layers on the lower surface and 3 to 4 layers on the upper surface using SPAR K81 elements (8-node, three-dimensional heat conduction elements) and K61 elements (6-node, three-dimensional heat conduction elements). The K61 elements were used only in the region where the modeled TPS layers changed from four to three layers on the upper surface (see fig. 6). The SIP was modeled by one layer of SPAR K81 elements.

A small one-dimensional thermal model for WS 240 bay 3 was used to determine the effect of the number of modeled TPS layers on the solutions. The lower skin peak temperature difference between 10 and 15 layer modeling was found to be only 0.8 percent; thus, modeling the lower surface TPS in 10 layers was considered quite adequate.

Because of the existence of gaps in the reusable surface insulation (RSI), heat conduction in both HRSI and LRSI was permitted only in the RSI thickness direction. To account for gap heating between the RSI tiles, the thickness of RSI was reduced to 80 percent of its original thickness. Aerodynamic surfaces were modeled using one layer of K41 elements of unit thickness to provide source heat generation. For the external and internal radiant heat energy exchanges, a layer of SPAR R41 elements (4-node thermal radiation exchange elements) was attached to the outer surface of the TPS and the exposed aluminum surfaces. For the spar webs with two sides exposed (lying between bays 1 and 2, 2 and 3, and 3 and 4), one layer of R41 elements was used for each exposed surface. Only one SPAR R41 element was used to represent radiation into space (see fig. 6). The size of the space R41 element was conveniently chosen so that it had unit length in the vertical direction and a width equal to the spanwise width of the wing segment. Because the surface areas were so small, thermal radiation exchanges were ignored at the rib cap shear webs

and rib trusses. Outer surfaces of the forward and rear spar webs were totally insulated. Internal convection and external convective cooling (negligible during reentry) were ignored.

Modeling of wing segment bound by WS 328 and WS 342.5 (fig. 4) was quite similar to the previous case. For this wing segment, TPS was modeled in 13 layers on the lower surface and 5 layers on the upper surface. Both the lower and upper TPS thicknesses were reduced to 80 percent of their original thicknesses to account for the gap heating. The three-dimensional thermal model for the wing segment shown in figure 7 has a total of 915 joint locations.

Modeling of FS 877 was two dimensional. Because it is symmetrical, only one-half of the fuselage cross section was modeled. The SPAR thermal model for FS 877 is shown in figure 8. The model has a total of 605 joint locations. The T-stiffener and hat-stringer-reinforced skins were represented by equivalent smooth skins with proper effective thicknesses. The equivalent skins, glove honeycomb core sandwich plate skins, bay door composite skins, longerons, vertical wall between the two lower longerons, torque box, and top centerline beam were modeled using SPAR K21 elements. The glove honeycomb core was modeled using SPAR K41 elements. The bay door honeycomb core was modeled using both SPAR K41 and K31 elements (3-node, two-dimensional heat conduction elements). The TPS was modeled in 10 layers using SPAR K41 elements.

To account for gap heating, the TPS thickness was reduced to 80 percent of its original thickness. Heat conduction in both HRSI and LRSI was allowed only in the RSI thickness direction to account for the existence of gaps betwen the RSI tiles. Heat conduction in FRSI was two dimensional. Both the SIP and the RTV heat sinks were modeled using SPAR K41 elements. To provide aerodynamic heating, the aero-surface was modeled using SPAR K21 elements for source heat generation. SPAR R21 elements (2 node thermal radiation exchange elements) were attached to the TPS outer surface and the exposed structural surfaces to handle both external and internal radiation heat exchange. Radiation to space was modeled using just one SPAR R21 element of unit length. Radiation exchange inside the torque box was neglected, and the cargo bay was assumed to be empty. Internal convection and external convective cooling (negligible during reentry) were not taken into account.

AERODYNAMIC HEATING

The external heat inputs to the thermal models were computed by a NASA computer program called THEOSKN using the velocity-altitude-angle-of-attack time history of the nominal STS-1 trajectory given in figure 1. The THEOSKN program solves the one-dimensional thin skin heating equation and computes time histories for surface temperature, heat transfer coefficients, heating rates, and skin friction. Real gas properties of air were used in all calculations.

Representative heating rate calculations at WS 240 are shown in figure 9. Three cases of heat inputs were generated: turbulent flow for both the lower and upper surfaces, laminar flow for both the lower and upper surfaces, laminar flow for the lower surface and the upper surface of bay 1, and separated flow for the upper surfaces of bays other than bay 1. The laminar heating

rates (dashed lines in fig. 9) were computed by Eckert's reference enthalpy method (ref. 2) and the turbulent heating rates (solid lines in fig. 9) were computed by the theory of van Driest (ref. 3). For both cases, a Reynolds analogy factor of 1.12 was used. The local flow conditions were computed by the oblique shock theory and the Prandtl-Meyer expansion theory. The initial wedge angle was taken to be the angle between the tangent to the wing skin (TPS surface) and the horizontal line passing through the stagnation point, which is parallel to the centerline of the shuttle. The flow distance was taken to be the chordwise distance as measured from the leading edge of the wing. The laminar and turbulent heating rates shown for the upper surface were computed by the same procedure used to calculate the lower surface heating rates, except that the flow expansion was limited in such a way that the local static pressure did not go below three-tenths of the free-stream static pressures. Finally, the separated flow heating rates for the upper surface (broken lines in fig. 9) were the estimated heating rates. For this analysis, the separated flow heating rates were taken to be one-half of the calculated heating rates of the attached laminar flow.

For WS 328, only one case of heat input was generated (fig. 10), namely, laminar flow for the lower surface and the upper surface of bay 1, and separated flow for the upper surfaces of bays 2 and 3. Calculation of the heating rates followed the same procedures used in the calculation of the laminar and separated flow heating rates for WS 240.

Heating rates calculated at FS 877 are shown in figure 11 for five typical locations: the lower centerline (point 1), the glove lower surface (point 2), the upper glove surface (point 3), the sidewall surface (point 4), and the upper centerline (point 5). Two cases of heat inputs were generated for the fuselage thermal model: turbulent flow on the fuselage belly surface, separated flow on the glove upper surface, and laminar/turbulent transition flow on both the sidewall surface and the bay door surface (80 percent TPS thickness); and laminar flow on the fuselage belly and the glove lower surfaces, separated flow on both the glove upper surface and the sidewall surface, and laminar flow on the bay door surface (80 percent TPS thickness).

The heating rates shown by the solid line for the lower centerline (point 1) were computed by the turbulent swept-cylinder theory of Beckwith and Gallagher (ref. 4), and the values shown by the dashed curves were computed by the laminar swept-cylinder theory of Fay and Riddell (ref. 5). The heating rates for the glove lower surface (point 2) were calculated using the method described above; however, the computed values were increased by 20 percent as suggested by results from shuttle wind tunnel tests. The upper glove surface (point 3) was known to be in a low heating separated flow region. Measured results for the similar geometry of the X-15 airplane during a reentry flight (ref. 6) showed the lower surface heating to be about 30 times the upper surface heating. Therefore, the heating rates for the upper glove surface were estimated by taking one-thirtieth of the heating rates calculated for the lower glove surface.

For the sidewall surface (point 4), it was not known if the flow was attached or separated; consequently, two calculations were made. The upper curve represents values calculated assuming attached laminar flow with transition to attached turbulent flow at a Reynolds number of 5×10^5 (at time = 1400 seconds from reentry). These heating rates were calculated using the flat-plate theories of Eckert's reference enthalpy method and van Driest for laminar and turbulent flow, respectively. A flow distance of 0.61 meter (2 feet) was used, and the flow conditions were assumed

to be equal to free-stream values. The separated flow heating rates were assumed to be one-tenth of the heating rates of the laminar attached flow.

The heating rates represented by the upper curve for the upper centerline (point 5) were calculated assuming attached laminar flow with transition to turbulent flow at a Reynolds number of 5×10^5 (at time $\approx$ 1000 seconds from reentry). For these calculations the local static pressures were assumed to be equal to one-half of the free-stream static pressures and the flow length was measured from the attachment point on the sidewall of the fuselage. The heating rates shown by the lower curve were computed assuming laminar flow with local pressures equal to one-fourth of the free-stream values. For both cases the flat-plate heating theories of Eckert's reference enthalpy and van Driest were used for laminar and turbulent calculations, respectively.

For more detailed discussion on the calculation of heating rates for the wing and the fuselage, see reference 7.

RADIATION EXCHANGE

For both the external and the internal thermal radiation exchanges, all the view factors were calculated from the equation (ref. 8)

$$A_i F_{ij} = A_j F_{ji} \tag{1}$$

where A_i is surface area of radiation exchange element i and F_{ji} is view factor, defined as the fraction of radiant heat leaving element j incident on element i. In the calculation of view factors for the external radiation exchanges (considering that element i represents the space element and element j any radiation exchange element on the wing or fuselage surface), F_{ji} was taken to be unity; therefore, $F_{ij} = \frac{A_j}{A_i}$ according to equation (1). In the view factor calculations for the fuselage internal radiation exchanges, each radiation exchange element was set to receive not only from the other elements but also from mirror images of all elements. In other words, the entire fuselage cross section was used to compute the fuselage internal radiation view factors. Values of emissivity and reflectivity used to compute radiant heat fluxes were:

Surface	Emissivity	Reflectivity
Windward	0.85	0.15
Leeward	0.80	0.20
Internal Structure	0.667	0.333
Space	1.0	0

The initial temperature distribution used in the analysis was obtained from the shuttle manufacturer. The effect of neglecting internal radiation was investigated using a small, three-dimensional thermal model for WS 240 bay 3, assuming total insulation from neighboring bays.

TRANSIENT THERMAL SOLUTIONS

The SPAR thermal analysis finite element computer program was used in the calculation of temperature time histories at all joint locations of the thermal models. The SPAR program used the approach described below to obtain transient thermal solutions.

The transient heat transfer matrix equation

$$(K_k + K_r)T + C\dot{T} = Q + R \tag{2}$$

where

K_k = conduction matrix
K_r = radiation matrix
T = temperature
C = capacitance matrix
$[\dot{}]$ = time derivative
Q = source load vector
R = radiation load vector

was integrated by assuming that the temperature vector T_{i+1} at time step t_{i+1} can be expressed as

$$T_{i+1} = T_i + \dot{T}_i \Delta t + \frac{1}{2!}\ddot{T}_i \Delta t^2 + \frac{1}{3!}\dddot{T}_i \Delta t^3 + \cdots \tag{3}$$

where T_i is the temperature vector at time step t_i, and Δt is the time increment. The vector $\dot{T}$ is determined directly from equation (2); i.e.,

$$\dot{T} = -C^{-1}(K_k + K_r)T + C^{-1}(Q + R) \tag{4}$$

Higher order derivatives are obtained by differentiating equation (2) according to the assumption that (1) material properties are constant, (2) Q varies linearly with time, and (3) R is constant over Δt:

$$\ddot{T} = -C^{-1}(K_k + 4K_r)\dot{T} + C^{-1}\dot{Q} \tag{5}$$

$$\dddot{T} = -C^{-1}(K_k + 4K_r)\ddot{T} + 4\dot{K}_r\dot{T} \tag{6}$$

etc.

In the present computations, the Taylor series expansion (eq. (3)) was cut off after the third term. The pressure dependency of the TPS and SIP properties was converted into time dependency based on the nominal trajectory given in figure 1.

Time dependent properties were then averaged over "time intervals," which were taken to be 2 seconds. Temperature dependent properties were evaluated at the temperatures computed at the beginning of each time interval. Q, $\dot{Q}$, and R were computed every 2 seconds.

RESULTS AND DISCUSSION

TPS Surface Temperatures

Computed TPS surface temperature time histories at eight typical locations (four locations on the lower surface and four locations on the upper surface) at WS 240 are shown in figure 12. For the lower surface, the peak heating for all four bays took place at about 900 seconds from the reentry for both turbulent and laminar flow. Heating at bay 1 was most severe, with peak temperatures reaching 1243° C (2269° F) for turbulent flow and 899° C (1650° F) for laminar flow. For the upper surface, the maximum heating for all four bays occurred at 1200 seconds for turbulent flow and at 1000 seconds for both laminar and separated flow. Again, the upper surface of bay 1 experienced approximately 310° C (590° F) for both turbulent and laminar flow.

The calculated TPS surface temperature time histories for WS 328 are shown in figure 13. The temperatures for the lower and the upper surfaces reached their peak values at t = 900 seconds and t = 1000 seconds respectively. Bay 1 was heated most severely and the peak temperatures there reached 873° C (1604° F) for the lower surface and 368° C (695° F) for the upper surface.

Calculated TPS surface temperature time histories at five locations at FS 877 are shown in figure 14. Except for the fuselage sidewall (point 5), the curves for all locations (points 1 to 4) have plateaus lying between 400 seconds and 1000 seconds. Heating was most severe at the lower glove surface (point 2) where the peak temperature was 919° C (1687° F) for turbulent flow and 707° C (1304° F) for laminar flow.

Structural Temperatures

Predicted aluminum skin temperature time histories at eight locations at WS 240 are shown in figure 15 for the three heating cases mentioned earlier. The STS-1 flight data are also shown for comparison. Flight data for the time interval 0 to 1178 seconds were not available because of the telemetering "blackout." Only data for the bay 3 lower skin were available, which were obtained from on-board instrumentation. For the entire lower skin and the bay 1 upper skin, the flight data correlate better with the laminar flow curves for 80 percent TPS thickness than with the laminar flow curves for 100 percent TPS thickness and turbulent flow curves, reflecting the effect of TPS gap heating and the fact that the actual flow was laminar. The measured results for the upper skins of bays 2 and 4 compare better with the separated flow curves (100 percent FRSI thickness, without gap heating) than with the laminar and turbulent flow curves, showing flow separation in the actual flight. No acceptable flight data were obtained for the upper skin of bay 3. The increasing deviation of the flight data for the lower skins from the laminar flow curves for 80 percent TPS thickness may be due to internal convection and to external convec-

tive cooling, which were neglected in the analysis. The continuous increase of the measured temperatures for the upper skins of bays 2 and 4, starting at 100 seconds before touchdown, may also be due to internal convective heating from the lower skin.

Temperature time histories of the lower and upper spar caps at WS 240 and a rib cap at WS 254 are shown in figure 16. The flight data for the lower spar and rib caps of bay 3 closely follow the laminar flow curves for 80 percent TPS thickness up to 1800 seconds; beyond that point, like the lower skin data, they deviate from the curves. The measured temperatures for the rear lower spar cap (top right plot) are higher than the laminar flow curve for 80 percent TPS thickness. The lower predicted values may be due to the assumption of total insulation on the aft side of the rear spar web. Like the upper skin data, the flight data for the upper spar and rib caps correlate better with the separated flow curves (100 percent TPS thickness) than with the laminar and the turbulent flow curves. Again, the data show continuous heating after touchdown, suggesting possible convective heat transfer from the lower skin.

The chordwise temperature distributions of the aluminum skins at WS 240 are shown in figure 17 for profile time t = 1600 seconds. The "scalloped" shape reflects the drop in temperature at the spar caps. For the lower surface, the measured temperatures follow the laminar flow curve for 80 percent TPS thickness quite well except at the rear spar (see also top right plot, fig. 16). For the upper surface, the plot shows laminar flow on bay 1 and the effect of separated flow on bays 2, 3, and 4.

The time histories of the predicted and the flight measured WS 328 skin temperatures are shown in figure 18. The flight data were available for only three locations (i.e., lower skin at bays 1 and 3, upper skin at bay 2) and only for the time after t = 1178 seconds. For the lower skin, the flight data agree fairly well with the laminar flow curves (80 percent TPS thickness) after touchdown. However, before the touchdown the flight data show higher temperatures than predicted. The cause of difference for bay 3 may be that part of the flight profile might be turbulent or transitional flow, and the cause of difference for bay 1 may be due to the higher initial temperature in the actual flight. Unlike bay 3 data, which show continued cooling after landing, the bay 1 data show no cooling at all. This is due to heating from the upper skin, which is hotter than the lower skin (see fig. 19). For the upper skin (fig. 18), the flight data for bay 2 agree very nicely with the separated flow curve (80 percent TPS thickness) up to t = 1600 seconds. After that the measured temperature continues to increase, whereas the calculated temperature increases at a very low rate, reflecting possible convective heat transfer from the hotter lower skin. In figure 18, the laminar flow curves for 100 percent TPS thickness are also plotted to show the effect of gap heating. The chordwise distribution of WS 328 skin temperatures is shown in figure 19 for the profile time of 1600 seconds. For the lower surface, the measured temperatures are slightly higher than the calculated curve. For the upper surface the flight data point falls right on the calculated curve (80 percent TPS thickness).

The temperature time histories of the fuselage skins at five locations are shown in figure 20. The measured belly temperatures agreed with the laminar flow curve for 80 percent TPS thickness until about 1800 seconds; then the data show rapid cooling, which suggests possible convective heat transfer effect of the air mass inside the cargo bay and the effect of external convective cooling, which were neglected in the calculations. The lower glove measured value was far below the laminar flow

curve for 80 percent TPS thickness, which should be the theoretical lower bound for the attached flow. It is possible that the data are incorrect or that the flow conditions in this area are substantially different from what one would assume. The predicted temperatures for the sidewall and the upper longeron are rather poor because of uncertainty in the flow field from which the heat inputs were calculated (e.g., location of flow re-attachment point, etc.). No acceptable data were obtained for the upper glove skin temperatures.

The circumferential distribution of the fuselage structural temperatures is shown in figure 21 for profile time 1600 seconds. The "valleys" of the curves indicate the temperature drop at the heat sinks (structural junction points). The cargo bay outer skin was heated more than the aluminum skin even though the heat input there was relatively low, indicating poor conductivities of the bay door materials.

Effect of Internal Radiation

The effect of internal radiation was investigated for bay 3 of WS 240 assuming total insulation from the neighboring bays. The results shown in figure 22 are for Mission 3 heat input. With the effect of internal radiation taken into account, the temperatures of the lower and the upper skins were brought closer (especially after landing), and the peak temperature of the lower skin was reduced by approximately 39° C (70° F).

COMPARISON WITH FINITE DIFFERENCE SOLUTIONS

The conventional finite difference method was also used in the thermal analysis in order to verify the solutions obtained from the SPAR finite element method. For this purpose, two-dimensional finite element and finite difference thermal models were set up for WS 240. The two models are shown in figure 23. For the SPAR finite element model, the lower and the upper TPS were modeled in 10 and 3 layers respectively. For the finite difference model, the divided TPS sublayers changed in number stepwise along the chordwise direction. For the lower TPS, the number of sublayers changed between 13 and 8, while for the upper TPS, the number of sublayers changed between 4 and 1.

The time histories of the WS 240 aluminum skin temperatures predicted by the two methods are given in figure 24. The two methods predicted fairly close temperatures except for bay 1. For the present modeling, the SPAR finite element method gives slightly higher lower skin temperatures and lower slopes for the upper skin temperature curves. The chordwise distributions of aluminum skin temperatures at t = 1600 seconds predicted by the two methods are shown in figure 25. The two types of solutions agree fairly well except for bay 1. The relatively large differences between the two solutions at bay 1 may be attributed to the difference in TPS modelings in the two models. By making the two thermal models as identical as possible, the two types of solutions should converge.

For those who are familiar with the finite element structural analysis, SPAR is attractive because the finite element thermal modeling and the finite element structural modeling are quite similar.

CONCLUSIONS

A finite element thermal analysis computer program was used in the reentry heat transfer analysis of the space shuttle. Thermal models were set up for two typical wing cross sections and for a midfuselage cross section.

The comparison between calculated and measured temperatures for the wing was quite good if laminar flow was assumed for the lower surface and the bay 1 upper surface and if separated flow was assumed for the upper surfaces of bays other than bay 1. The differences that did exist could be caused by the following assumptions made in the thermal modeling: (1) the use of effective thicknesses for the TPS, stiffened skins, corrugated spar webs, and honeycomb core; (2) no internal convection and no external convective cooling; (3) initial temperatures and emissivities; and (4) total insulation on the outboard sides of WS 240 and WS 328, on the inboard sides of WS 254 and WS 242.5, and on the outer surfaces of both forward and rear spar webs.

For the fuselage, good agreement between the calculated and measured temperatures was obtained for the lower surface if laminar flow was assumed. Why the calculated and measured temperatures for the lower glove differed so greatly is not known. It is possible that the flight data were inaccurate or that the flow conditions in this area are substantially different from what one would assume. The difference between the prediction and the flight data for the upper fuselage surface is probably due to the very complex flow in this region— exactly where the flow is attached and/or separated is not known. Other causes of data/prediction discrepancies could be the following assumptions made in the thermal modeling of the fuselage: (1) the use of effective thicknesses for the TPS and stiffened skins; (2) no internal convection and no external convective cooling; and (3) initial temperatures, emissivities, and two-dimensional nature of the thermal model.

REFERENCES

1. Marlowe, M. B.; Moore, R. A.; and Whetstone, W. D.: SPAR Thermal Analysis Processors Manual, System Level 16. Volume 1: Program Execution. NASA CR-159162, Oct. 1979.

2. Eckert, E. R. G.: Survey of Boundary Layer Heat Transfer at High Velocities and High Temperatures. WADC-TR-59-624, Wright Air Development Center, Wright-Patterson AFB, Ohio, Apr. 1960.

3. van Driest, E. R.: The Problem of Aerodynamic Heating. Aeronaut. Engr. Rev., vol. 15, no. 10, Oct. 1956, pp. 26-41.

4. Beckwith, I. E.; and Gallagher, J. J.: Local Heat Transfer and Recovery Temperatures on a Yawed Cylinder at a Mach Number of 4.15 and High Reynolds Numbers. NASA TR R-104, 1961.

5. Fay, J. A.; and Riddell, F. R.: Theory of Stagnation Point Heat Transfer in Disassociated Air. J. Aeronaut. Sci., vol. 25, no. 2, Feb. 1958, pp. 73-85, 121.

6. Quinn, R. D.; and Olinger, F. V.: Heat-Transfer Measurements Obtained on the X-15 Airplane Including Correlations With Wind-Tunnel Results. NASA TM X-1705, 1969.

7. Gong, L.; Quinn, R. D.; and Ko, W. L.: Reentry Heating Analysis of Space Shuttle with Comparison of Flight Data. Computational Aspects of Heat Transfer in Structures, NASA CP-2216, 1982. (Paper no. 17 of this compilation.)

8. Sparrow, E. M.; and Cess, R. D.: Radiation Heat Transfer. McGraw-Hill Book Co., Inc., New York, 1978.

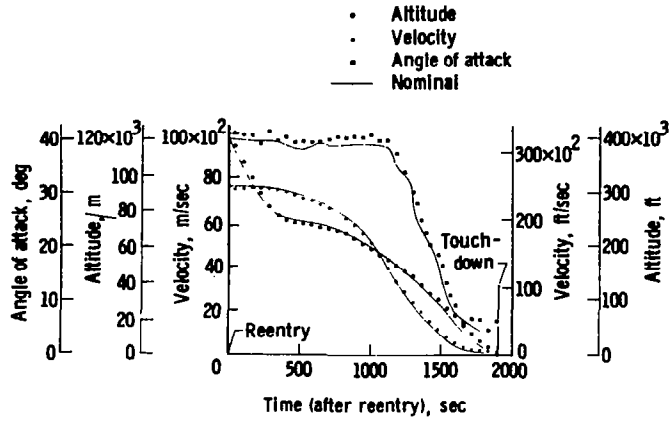

Figure 1. Nominal versus actual trajectory time history.

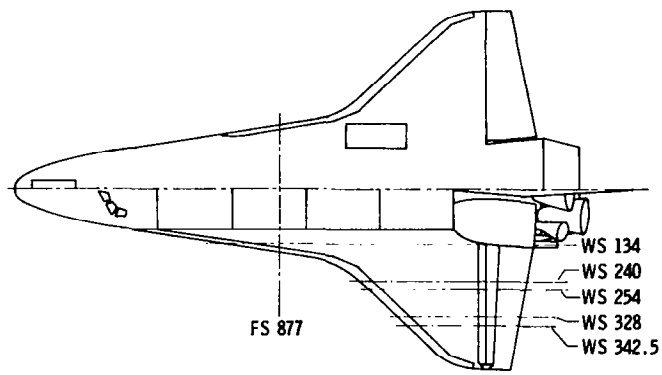

Figure 2. Locations of wing stations and fuselage stations.

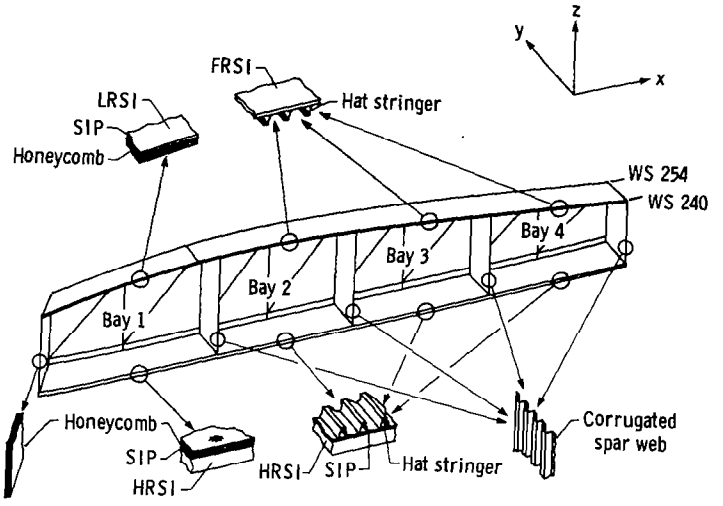

Figure 3. Geometry of wing segment between WS 240 and WS 254.

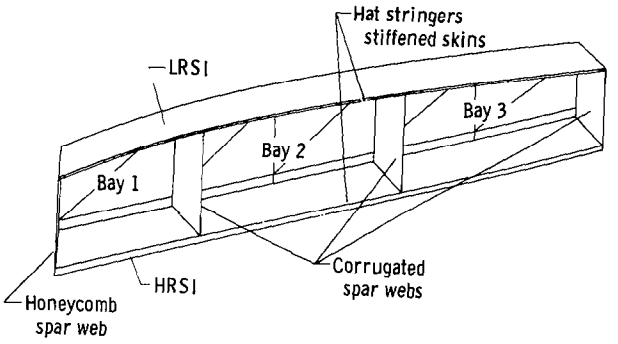

Figure 4. Geometry of wing segment between WS 328 and WS 342.5.

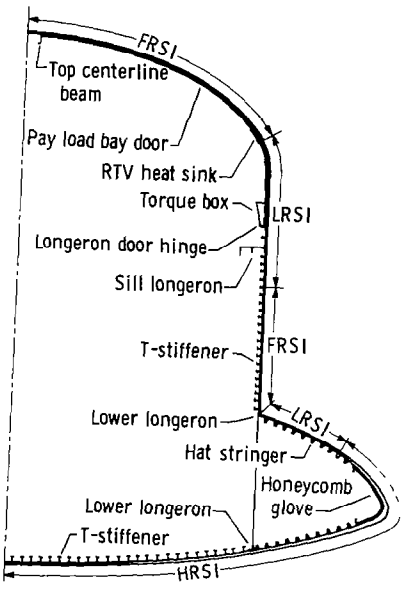

Figure 5. Geometry of fuselage cross section at FS 877.

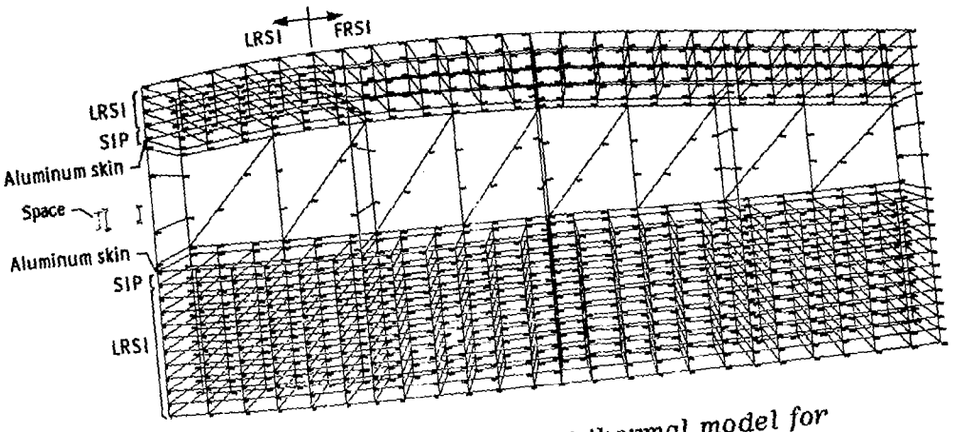

Figure 6. SPAR finite element thermal model for WS 240 (three-dimensional).

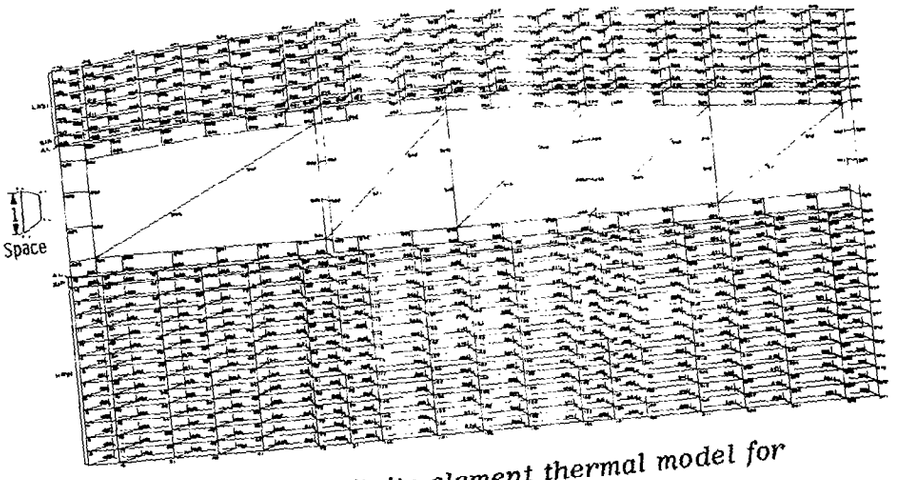

Figure 7. SPAR finite element thermal model for WS 328 (three-dimensional).

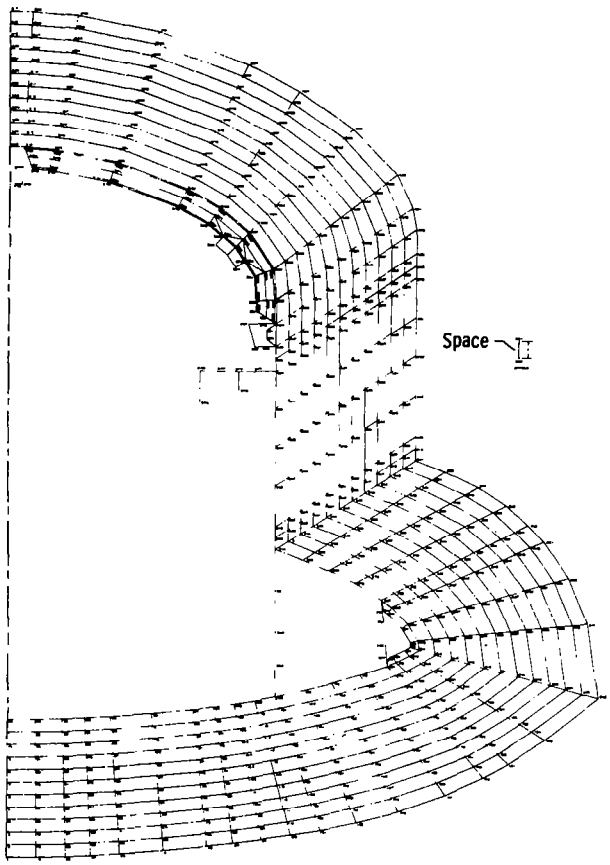

Figure 8. SPAR finite element thermal model for FS 877 (two-dimensional).

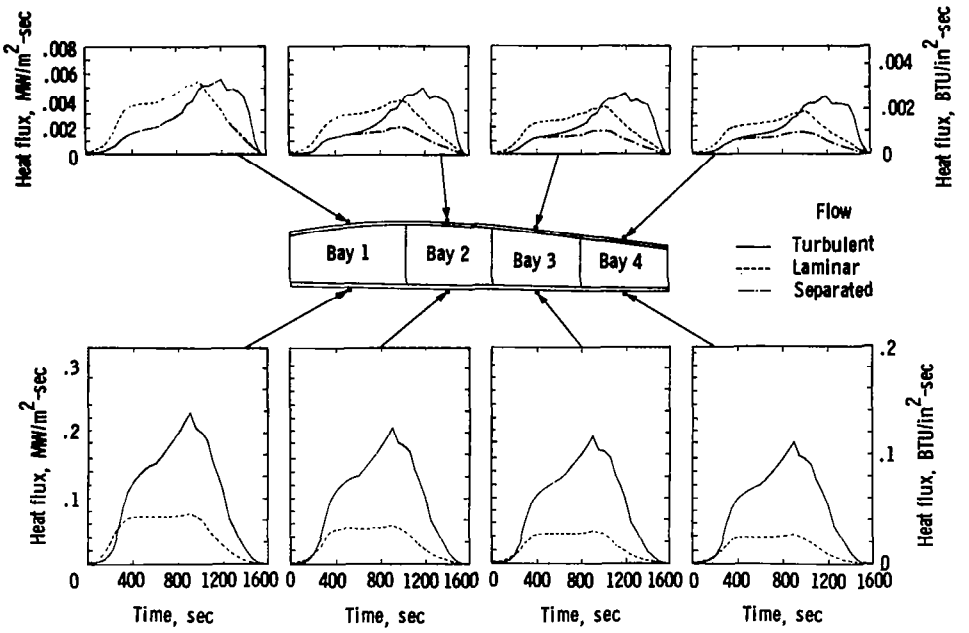

Figure 9. Surface heating rates at WS 240. STS-1 flight.

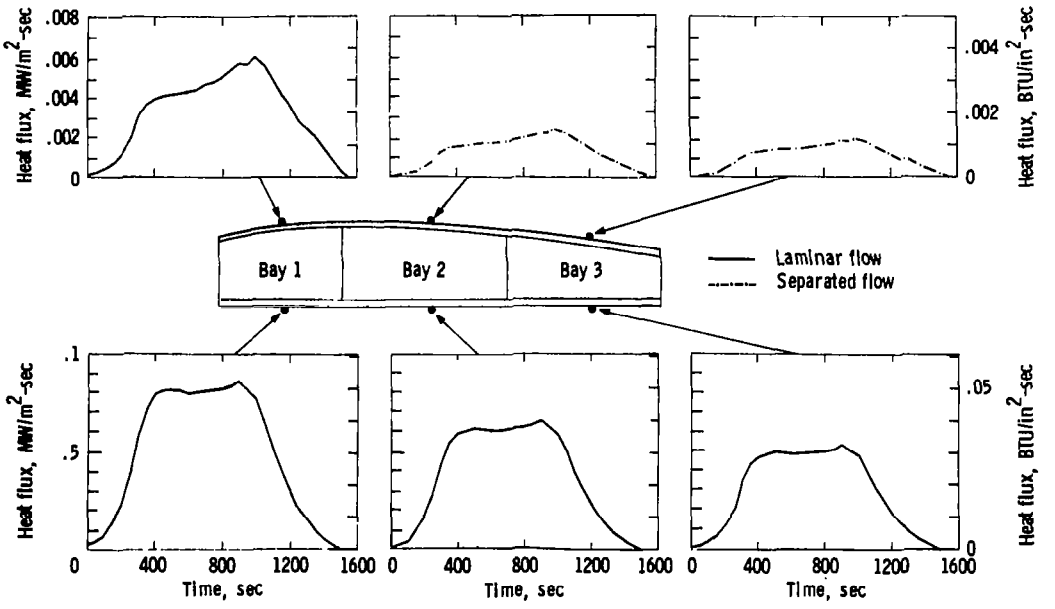

Figure 10. Surface heating rates at WS 328. STS-1 flight.

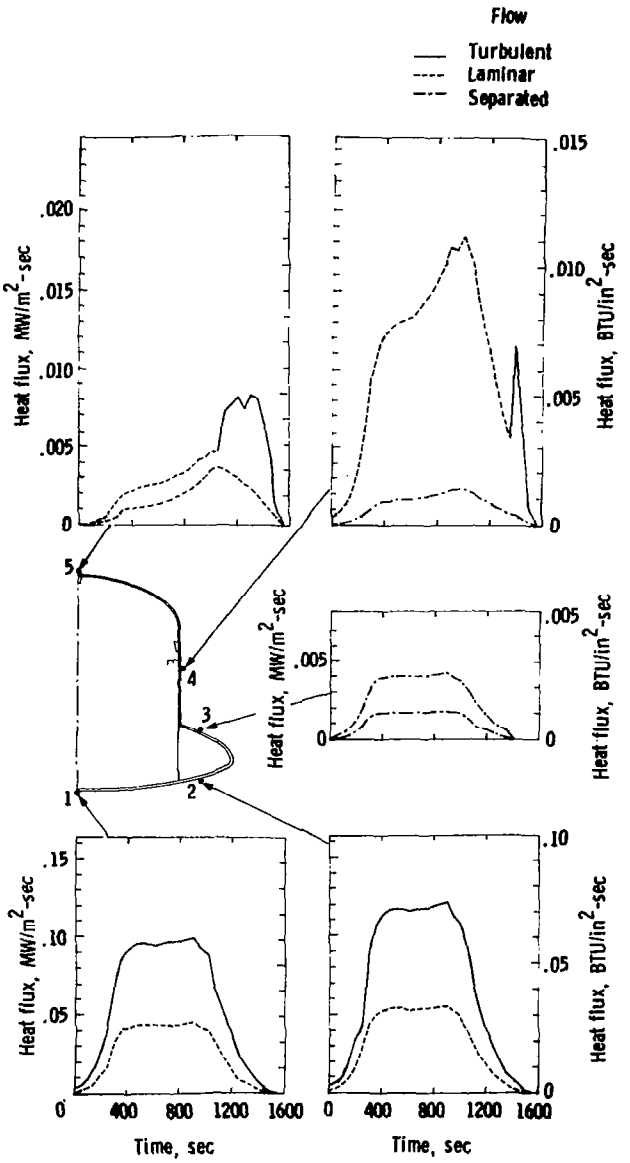

Figure 11. Surface heating rates at FS 877. STS-1 flight.

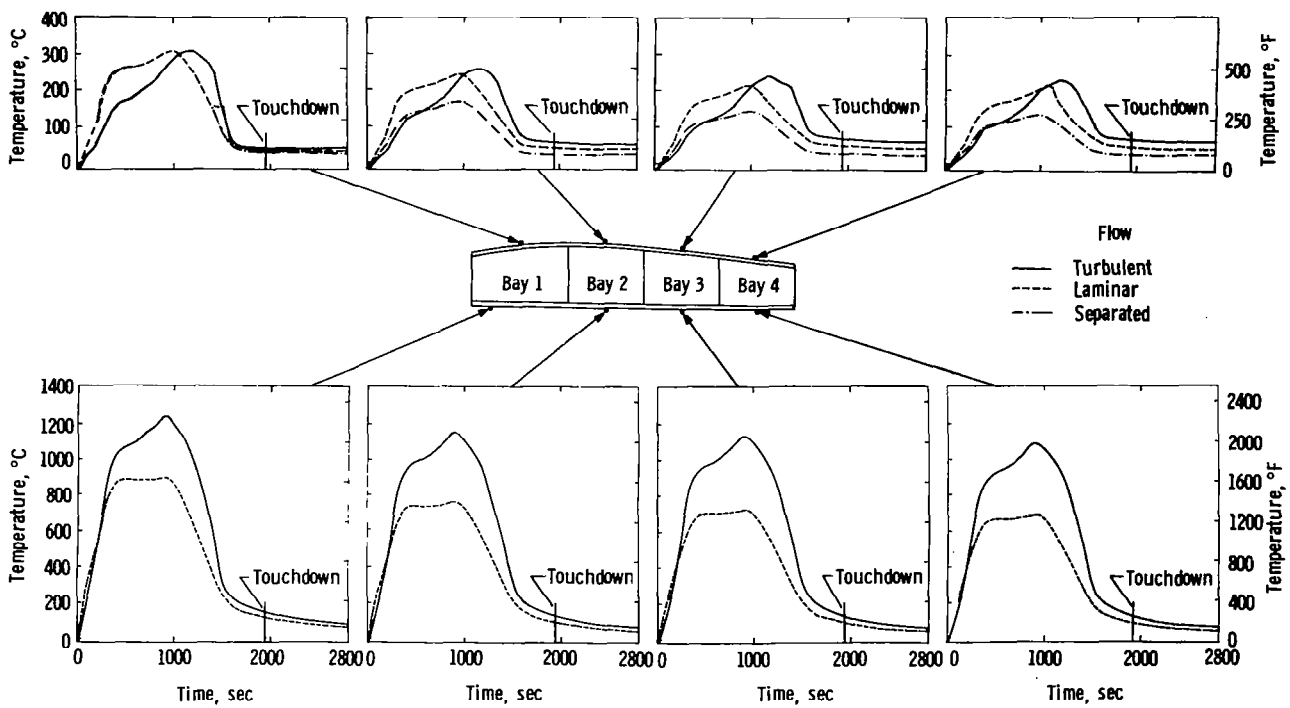

Figure 12. WS 240 TPS surface temperature time histories. STS-1 flight.

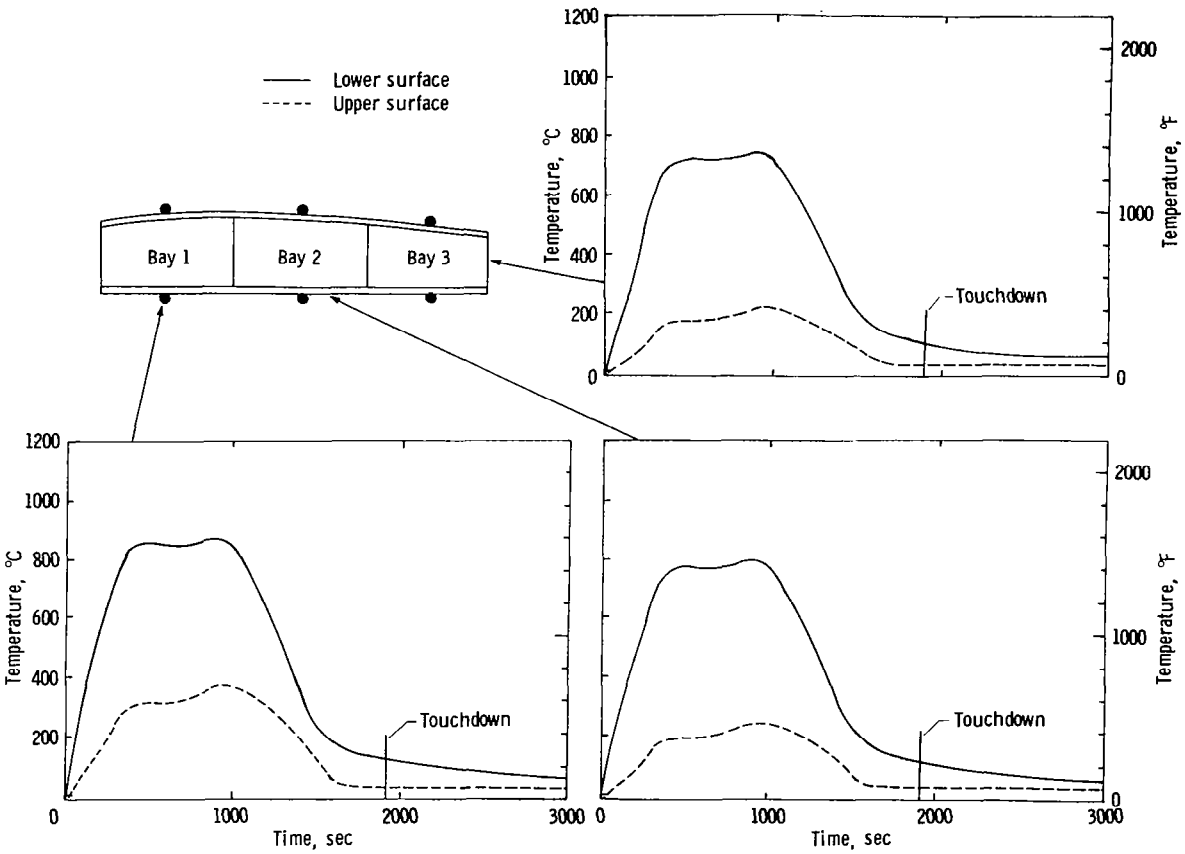

Figure 13. WS 328 TPS surface temperature time histories. STS-1 flight.

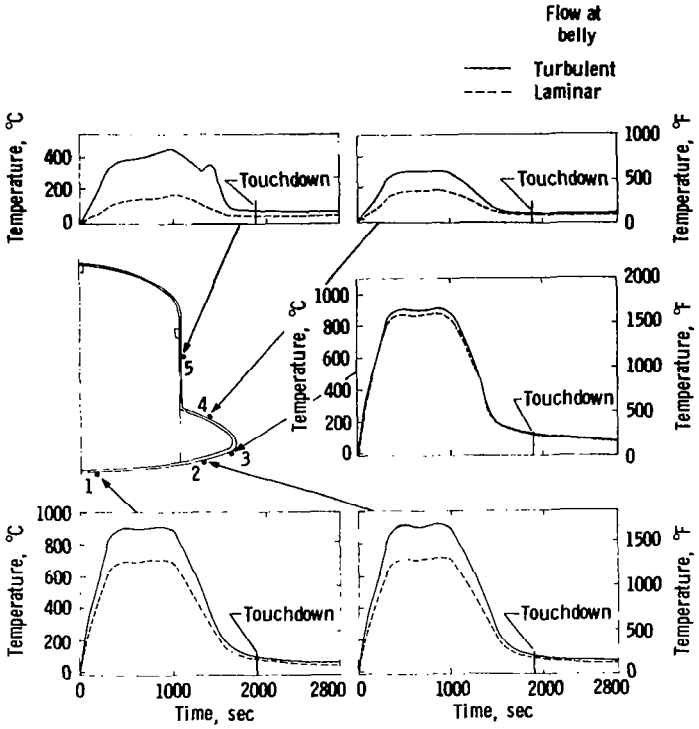

Figure 14. FS 877 TPS surface temperature time histories. STS-1 flight.

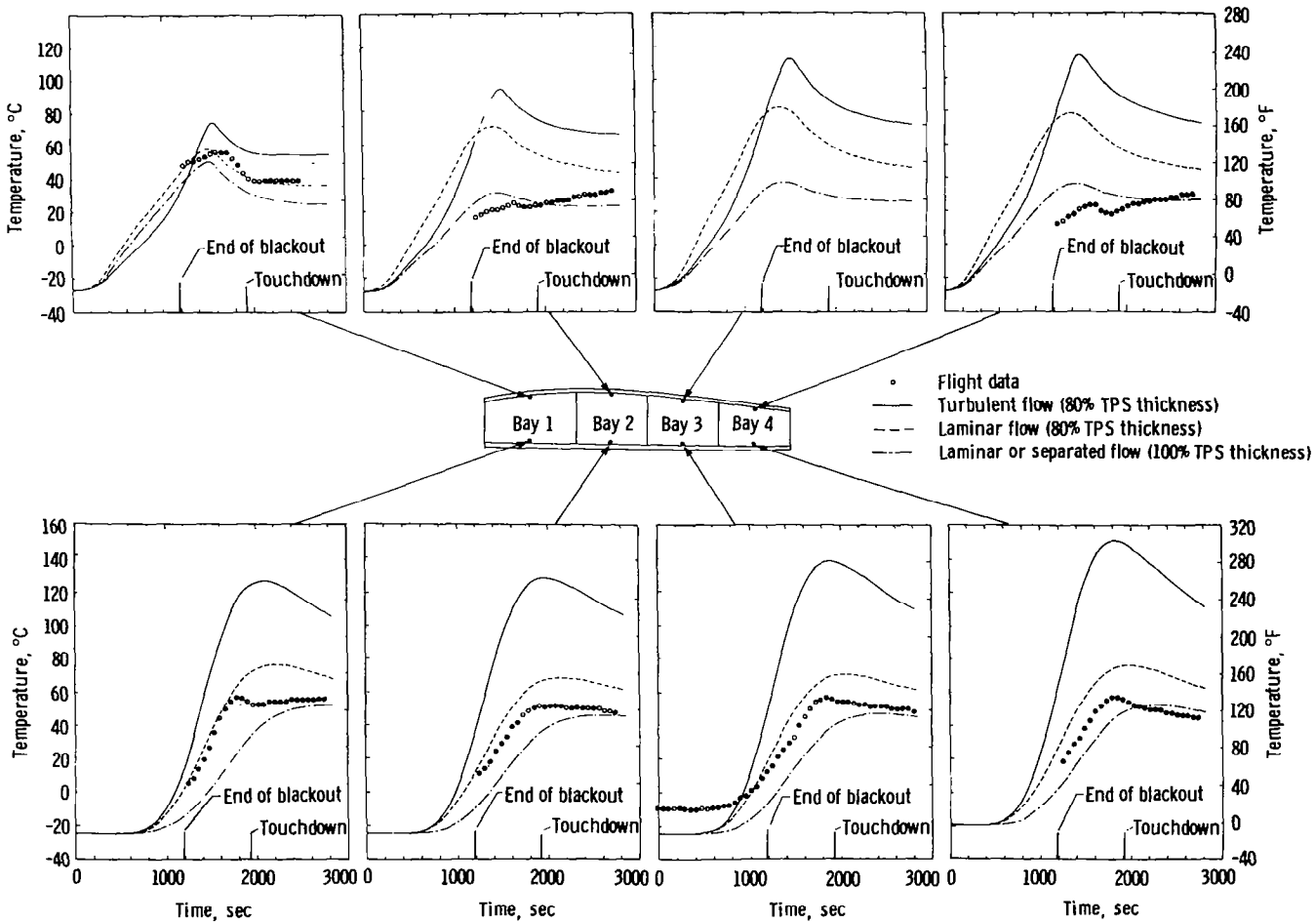

Figure 15. WS 240 aluminum skin temperature time histories. STS-1 flight.

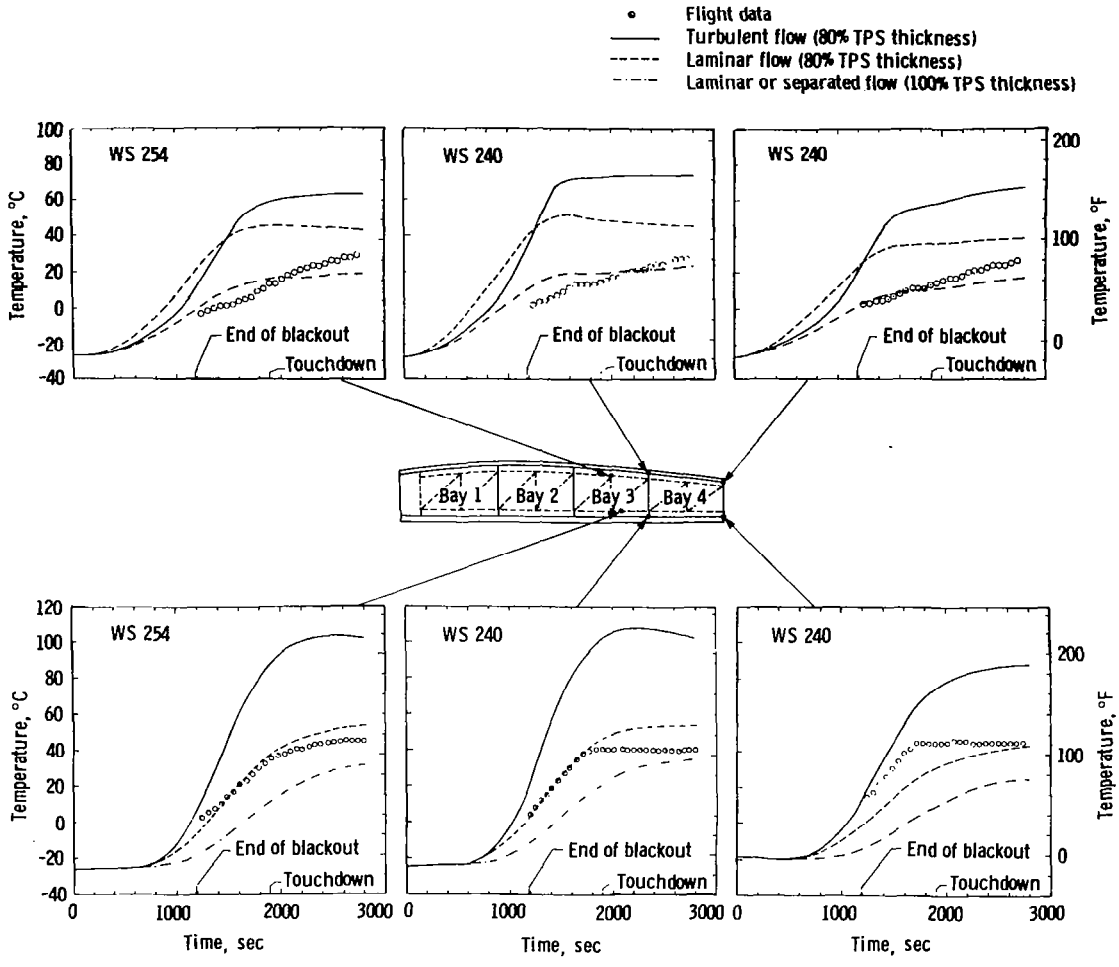

Figure 16. SPAR and rib caps temperature time histories. STS-1 flight.

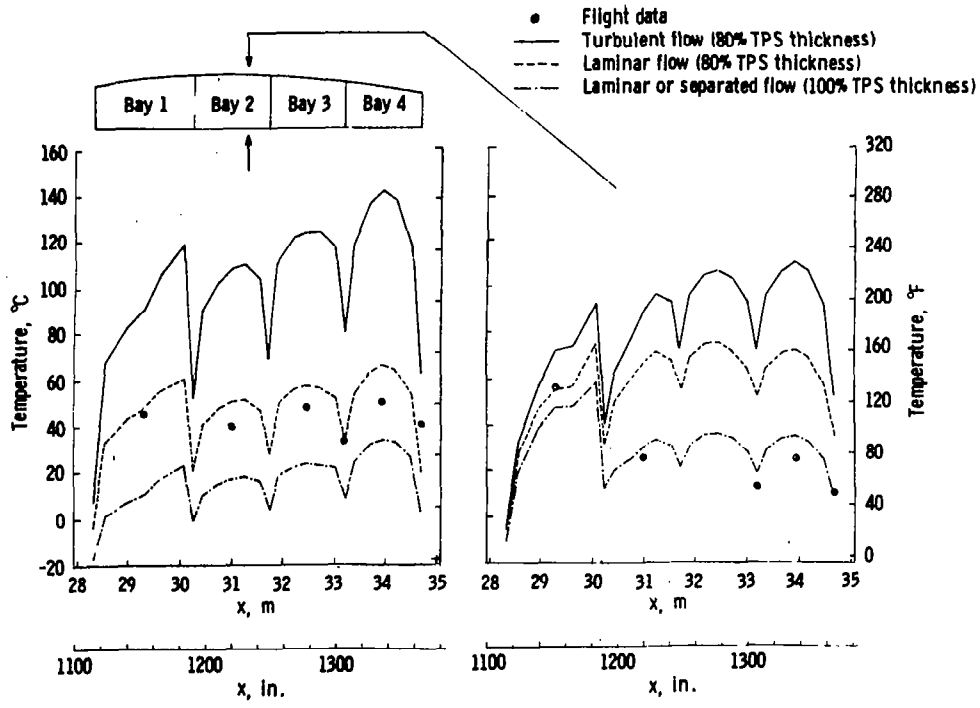

Figure 17. WS 240 chordwise distribution of the aluminum skin temperatures based on different surface heatings. Time = 1600 seconds.

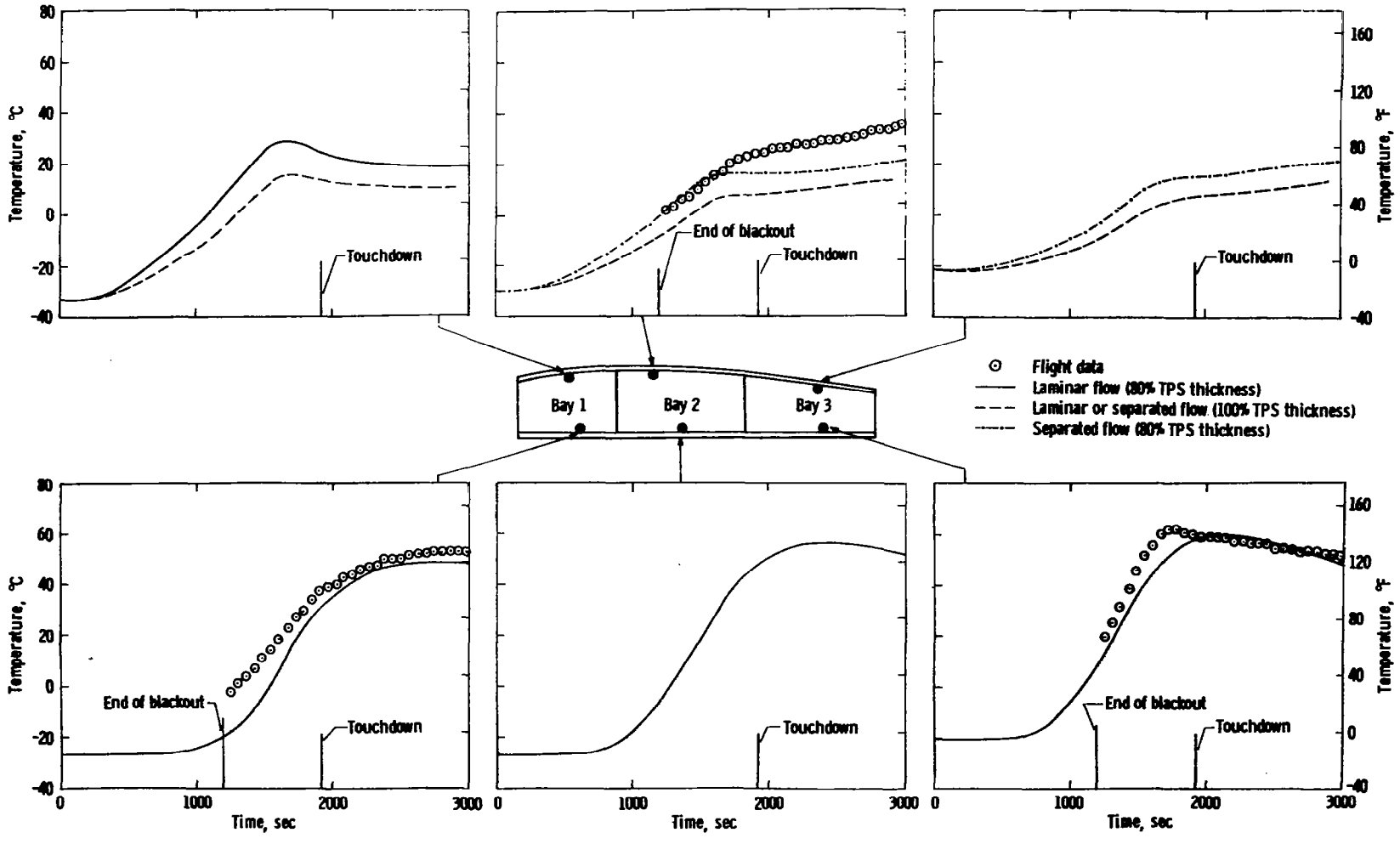

Figure 18. WS 328 aluminum skin temperature time histories. STS-1 flight.

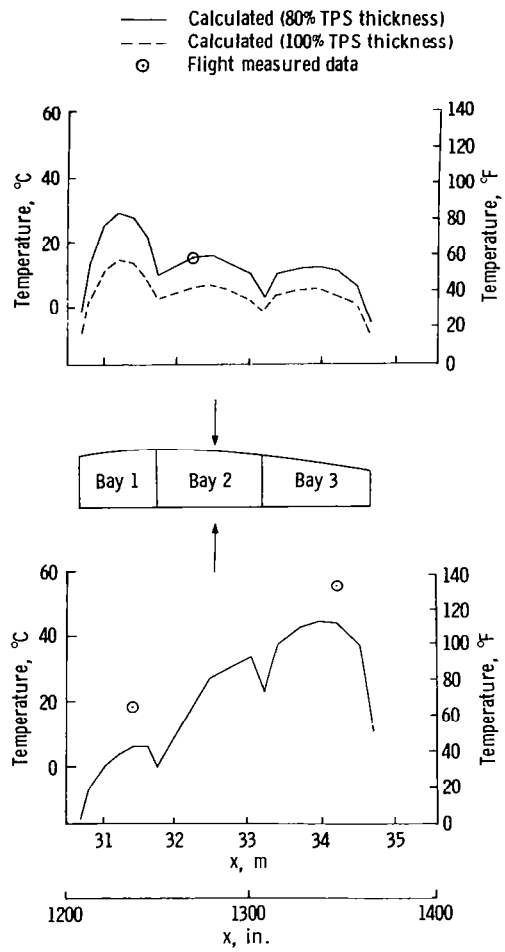

Figure 19. WS 328 chordwise distribution of the aluminum skin temperatures. STS-1 flight. Time = 1600 seconds.

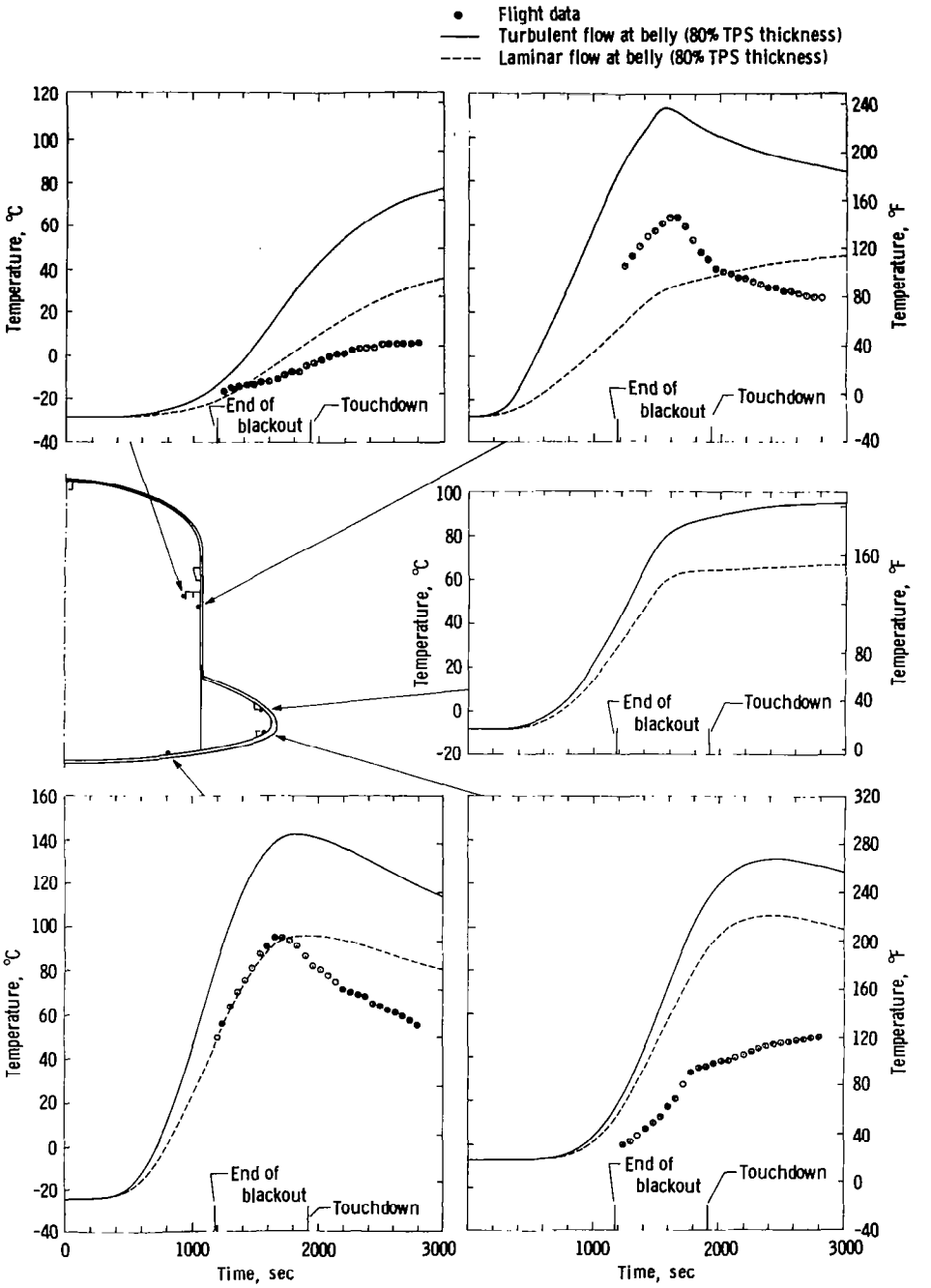

Figure 20. FS 877 aluminum skins temperature time histories. STS-1 flight.

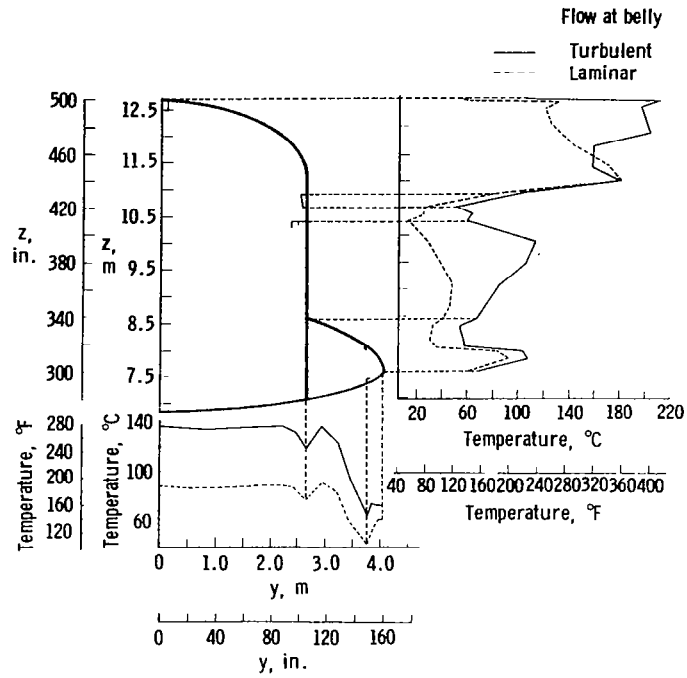

Figure 21. FS 877 circumferential distribution of the structural temperature. STS-1 flight. Time = 1600 seconds.

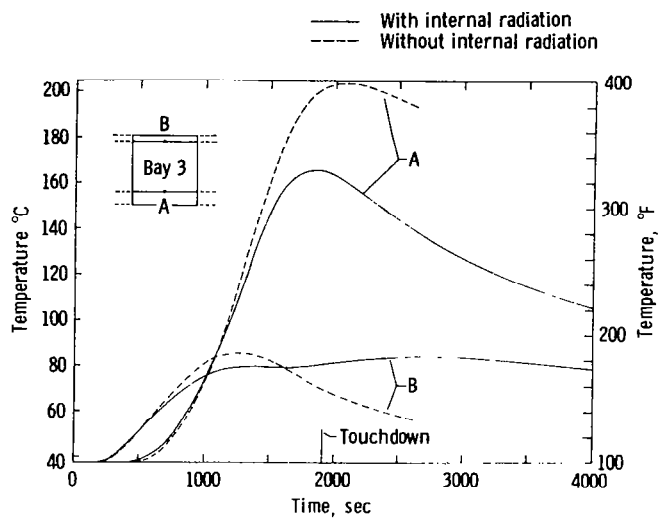

Figure 22. Effect of internal radiation on WS 240 bay 3 aluminum skin temperatures. Mission 3 heating.

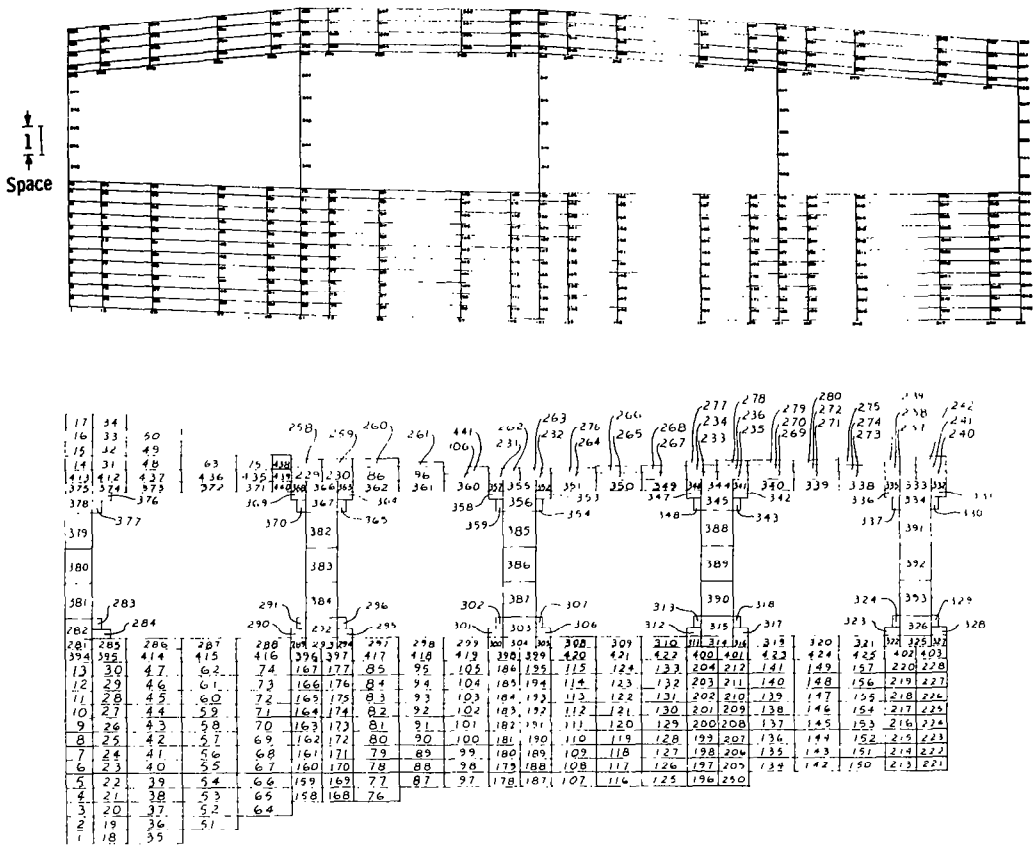

Figure 23. SPAR finite element thermal model and finite difference model for WS 240 (two-dimensional).

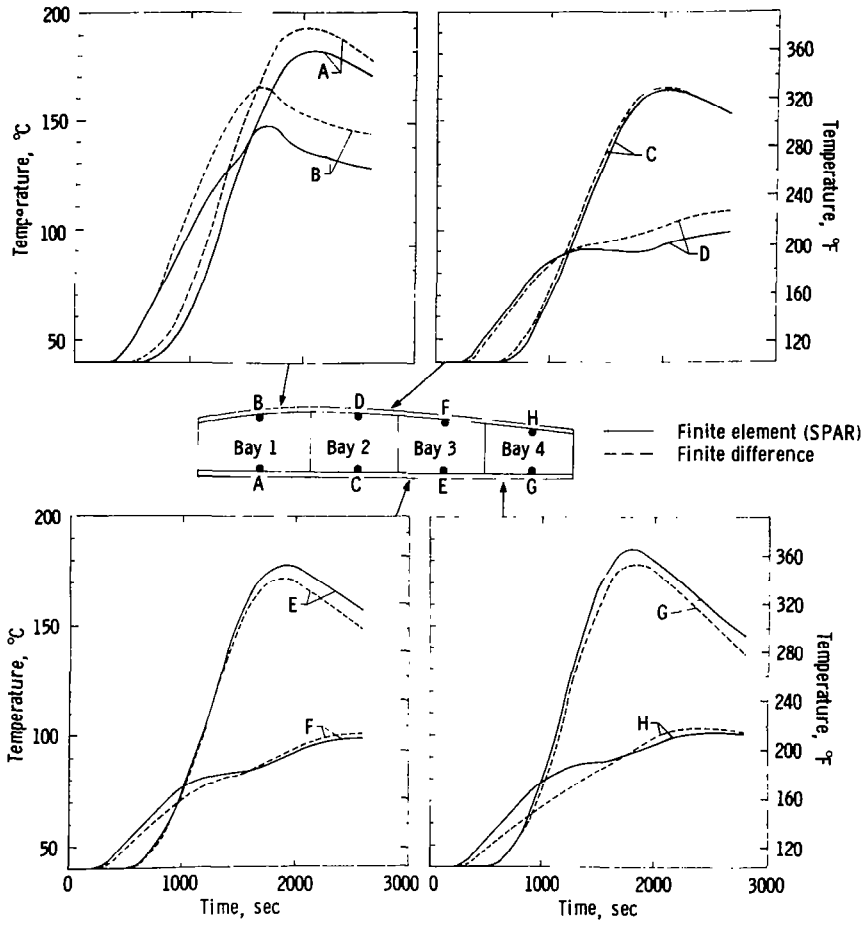

Figure 24. WS 240 aluminum skin temperature time histories predicted by finite element and finite difference methods. Mission 3 heating.

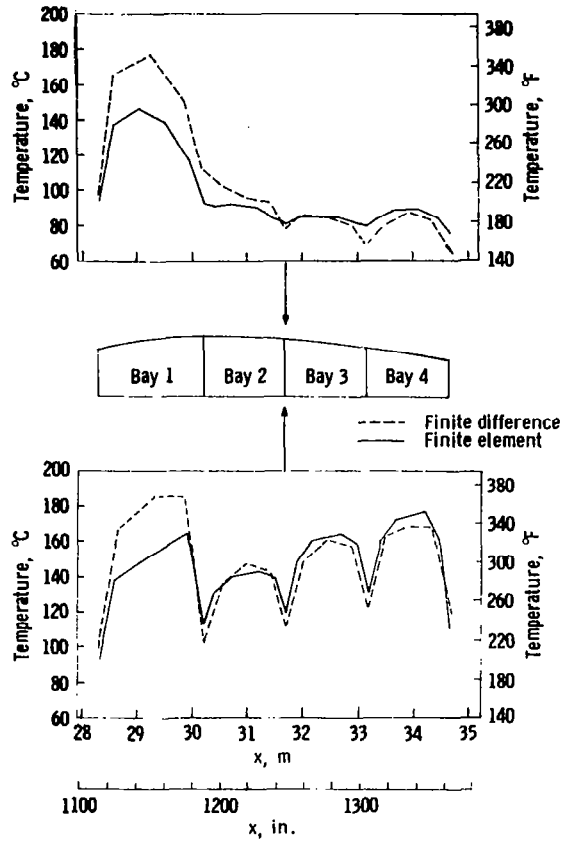

Figure 25. WS 240 chordwise aluminum skin temperature distributions predicted by finite element and finite difference methods. Time = 1600 seconds. Mission 3 heating.